ACS OMEGA

Open Access

http://pubs.acs.org/journal/acsodf

Article

Ultrafast Heating-Induced Suppression of *d*-Band Dominance in the Electronic Excitation Spectrum of Cuprum

Zhandos Moldabekov,* Thomas D. Gawne, Sebastian Schwalbe, Thomas R. Preston, Jan Vorberger, and Tobias Dornheim

Cite This: *ACS Omega* 2024, 9, 25239−25250

Read Online

ACCESS | Metrics & More | Article Recommendations

ABSTRACT: The combination of isochoric heating of solids by free-electron lasers (FELs) and in situ diagnostics by X-ray Thomson scattering (XRTS) allows for measurements of material properties at warm dense matter (WDM) conditions relevant for astrophysics, inertial confinement fusion, and materials science. In the case of metals, the FEL beam pumps energy directly into electrons with the lattice structure of ions being nearly unaffected. This leads to a unique transient state that gives rise to a set of interesting physical effects, which can serve as a reliable testing platform for WDM theories. In this work, we present extensive linear-response time-dependent density functional theory (TDDFT) results for the electronic dynamic structure factor of isochorically heated copper with a face-centered cubic lattice. At ambient conditions, the plasmon is heavily damped due to the presence of d-band excitations, and its position is independent of the wavenumber. In contrast, the plasmon feature starts to dominate the excitation spectrum and has a Bohm−Gross-type plasmon dispersion for temperatures $T \geq 4$ eV, where the quasi-free electrons in the interstitial region are in the WDM regime. In addition, we analyze the thermal changes in the d-band excitations and outline the possibility to use future XRTS measurements of isochorically heated copper as a controlled testbed for WDM theories.

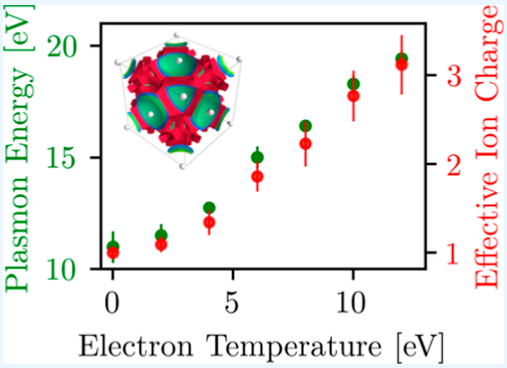

1. INTRODUCTION

The study of matter under extreme densities and temperatures has emerged as a highly active research field due to the availability of modern laser facilities equipped with various X-ray diagnostic techniques. High-power laser facilities are routinely being used to explore the physics and chemistry at conditions relevant to planetary astrophysics,[1−3] inertial confinement fusion,[4−6] and to explore new exotic materials.[7] For example, using lasers for heating and compression allows one to measure macroscopic properties such as the equation of state.[8−13] In addition, ultrashort X-ray free-electron laser (XFEL) capabilities, e.g., at the European XFEL[14] and LCLS,[15] have opened the way to study phenomena on femtosecond time scales.[16] By heating the electrons without directly affecting the ions, an XFEL with a sub-100 fs duration provides a unique opportunity to generate and study a transient state with hot electrons within the unperturbed crystal structure of the ions.[17,18] In these experiments, the X-ray Thomson scattering (XRTS) technique[19] can then be used to probe the electronic structure of a given system by measuring its electronic dynamic structure factor (DSF), $S(\mathbf{q}, \omega)$, where $\mathbf{q}$ and ω are the change in momentum and frequency of the scattered photon.

In this way, it was shown that the laser-induced heating of electrons leads to the lattice instability and melting (disordering) of silicon due to the weakening of the interionic bonds.[20,21] In contrast to semiconductors, metals can remain stable under laser heating of the electrons and, strikingly, can even manifest a more rigid lattice structure. For example, Descamps et al.[17] have recently reported the observation of a stable gold crystal lattice where the electrons have been heated by the FEL to a few electronvolts. In this experiment, a signature of phonon hardening has been observed, whereby the bonds stiffen between atoms. This effect was earlier predicted by ab initio Kohn−Sham density functional theory (KS-DFT) calculations[65] of the hot electrons within the cold ionic lattice using the local density approximation (LDA) for the exchange−correlation (XC) functional. A second example for the successful utilization of KS-DFT for predicting the properties of solids with laser-excited electrons is the

Received: March 26, 2024
Revised: May 8, 2024
Accepted: May 20, 2024
Published: May 29, 2024

calculation of the XRTS spectrum of an isochorically heated aluminum foil by Mo et al.[21] based on linear-response time-dependent DFT (LR-TDDFT) using an adiabatic LDA (ALDA) XC kernel. The same combination of LR-TDDFT with ALDA was shown to accurately describe the XRTS spectrum of aluminum at ambient conditions, where the plasmon was measured with ultrahigh resolution at the European XFEL.[22] Therefore, LR-TDDFT can be expected to yield accurate results for the electronic dynamic structure factor of isochorically heated metals across temperature regimes.

Very recently, Moldabekov et al.[23] have used this approach to study the effect of electronic heating on the order of a few electronvolts on the expected XRTS spectrum;[23] this has revealed an interesting red shift of the plasmon energy by 0.1 eV for aluminum and by 1 eV for silicon as a consequence of thermal excitations. In the case of aluminum, the effect is small and only manifests at small wavenumbers $q \lesssim 0.1$ Å^{-1}, making it very challenging to measure. For silicon, on the other hand, the plasmon shift of 1 eV at temperatures $T \simeq 2$ eV is well within experimental measurement capabilities.[22,24] However, the possible instability of the lattice due to the weakening of the interionic bonds[20,21] can be a serious obstacle in practice. Therefore, it is important to ask if such a heating-induced red shift prominently manifests itself in other metals that are stable under FEL radiation. Going back to aluminum, an additional thermally induced feature is the formation of a double plasmon peak as the region of Landau damping is shifted to lower wavenumbers upon increasing the electronic temperature.[23] This effect is similar to the formation of the double plasmon in the DSF of ground-state aluminum near the pair continuum.[25−27] These results show that thermal excitations in X-ray-driven solids can generate a variety of new features in the XRTS spectrum at a finite momentum transfer.

In the present work, we carry out extensive new LR-TDDFT calculations to explore the XRTS spectrum of isochorically heated copper. In contrast to simple metals, the effect of d-states dominates over plasmon-type excitations in the DSF of electrons in transition metals.[28,29] In gold and copper, excitations originating in the d-band lead to the formation of a prominent double peak structure at $\omega > \omega_p$ and a substantial broadening of the plasmon feature at $\omega = \omega_p$. Interestingly, the presence of the d-state excitations leads to a plasmon dispersion that is nearly independent of the wavenumber for both materials.[28,29] Here, we investigate in detail the interplay of these effects with thermal excitations on the DSF of copper at different temperatures, wavenumbers, and crystallographic directions. Indeed, thermal effects on the DSF are profound: we find an emerging collective plasmon excitation that becomes dominant over the d-band feature for $T \gtrsim 4$ eV and which starts to follow the familiar Bohm−Gross relation in this regime. In addition, we find a pronounced blue shift of the plasmon with increasing T, which is in stark contrast to other isochorically heated metals such as Al.[23] Finally, we discuss the possibility to use XRTS experiments with isochorically heated copper as a rigorous testbed for the theoretical modeling of warm dense matter (WDM)[30−32]—an extreme state that occurs in astrophysical objects[3,33−35] and which plays an important role, e.g., for inertial confinement fusion[4,6,36] applications.

The paper is organized as follows: in Section 2, we give an overview of the LR-TDDFT approach and provide computational details of our simulations. The results of the calculations are presented and discussed in Section 3. The paper is concluded by a summary of the main findings and an outlook over future works in Section 4.

2. LR-TDDFT APPROACH TO THE DYNAMICAL STRUCTURE FACTOR

2.1. Theoretical Framework. The intensity that is measured in an XRTS experiment is given by a convolution of the combined source-and-instrument function $R(\omega_s)$[12] and the electronic dynamic structure factor $S(\boldsymbol{q},\omega) = S(\boldsymbol{q}, -\Delta\omega)$ (with $\Delta\omega$ being the energy loss of the scattered photon)

$$I(\mathbf{q}, \Delta\omega_s) = S(\boldsymbol{q}, \Delta\omega) \times R(\omega_s) \tag{1}$$

where the latter accounts both for the finite width of the probing X-ray source and for all effects of the detector.[37] The momentum transfer $\mathbf{q}$ is determined from the scattering angle. The state-of-the-art is given by the European XFEL in Germany, where XRTS measurements with the capability of resolving electronic features with a resolution of up to $\delta\omega \sim 0.1$ eV have been recently demonstrated.[22]

To study the effect of thermal electronic excitations on the XRTS spectrum of X-ray-driven copper, we use the LR-TDDFT method with an adiabatic XC kernel. Indeed, LR-TDDFT constitutes the most common method to study the DSF of solids, and there is a vast body of dedicated literature, see, for example, ref 38 and references therein; here, we restrict ourselves to a concise overview of the main ideas.

As a first step, we consider the well-known fluctuation−dissipation theorem that connects the macroscopic dielectric function $\varepsilon_M(\boldsymbol{q},\omega)$ with $S(\boldsymbol{q},\omega)$[39,40]

$$S(\boldsymbol{q}, \omega) = -\frac{\hbar^2 q^2}{4\pi^2 e^2 n} \frac{1}{1 - e^{-\hbar\omega/k_B T}} \mathrm{Im}[\varepsilon_M^{-1}(\boldsymbol{q}, \omega)] \tag{2}$$

where n denotes the electronic number density, and e is the elementary charge. The term "macroscopic" indicates that $\varepsilon_M(\boldsymbol{q},\omega)$ describes the volume averaged response to an external perturbation.[41−43] It is computed by taking the diagonal part of the inverse microscopic dielectric matrix $\varepsilon_M^{-1}(\boldsymbol{q}, \omega) = [\varepsilon^{-1}(\boldsymbol{k}, \omega)]_{GG}$, where $\boldsymbol{q} = \boldsymbol{G} + \boldsymbol{k}$ (with $\boldsymbol{k}$ being in the first Brillouin zone) and $\boldsymbol{G}$ is a reciprocal lattice vector.[41,44] The latter is defined by the microscopic density response function[38]

$$\varepsilon_{\boldsymbol{G},\boldsymbol{G}'}^{-1}(\boldsymbol{k}, \omega) = \delta_{\boldsymbol{G},\boldsymbol{G}'} + \frac{4\pi}{|\boldsymbol{k} + \boldsymbol{G}|^2} \chi_{\boldsymbol{G},\boldsymbol{G}'}(\boldsymbol{k}, \omega) \tag{3}$$

The LR-TDDFT method allows one to compute $\chi_{\boldsymbol{G},\boldsymbol{G}'}(\boldsymbol{k}, \omega)$ in different approximations. The lowest rank corresponds to the so-called independent particle approximation (IPA). In the IPA, the Kohn−Sham (KS) orbitals and eigenenergies are used to calculate the density response function $\chi^0_{\boldsymbol{G},\boldsymbol{G}'}(\boldsymbol{k}, \omega)$ according to the ideal electron gas model.[45] Since the KS eigenenergies from the self-consistent ground-state (equilibrium state) calculations are employed, $\chi^0_{\boldsymbol{G},\boldsymbol{G}'}(\boldsymbol{k}, \omega)$ already has information about excitations between different orbitals. However, being computed using a formula for the ideal Fermi gas model, $\chi^0_{\boldsymbol{G},\boldsymbol{G}'}(\boldsymbol{k}, \omega)$ omits various correlation effects, such as screening due to the Hartree mean field, microscopic density inhomogeneities due to the field of the ions, etc. The inclusion of correlation effects leads to a

https://doi.org/10.1021/acsomega.4c02920
ACS Omega 2024, 9, 25239−25250

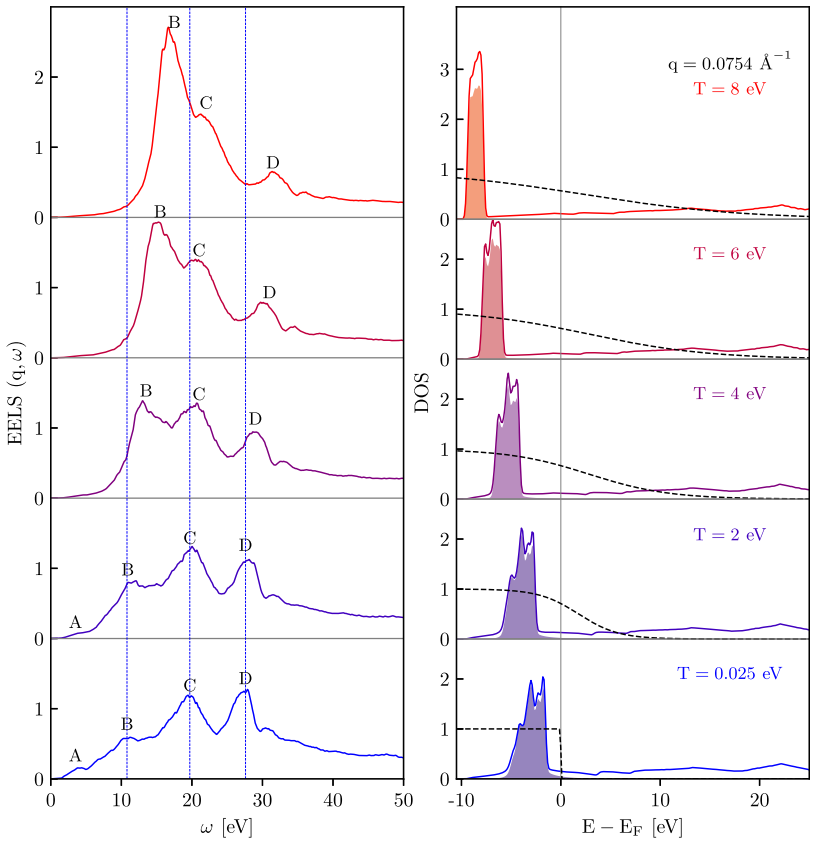

Figure 1. Left panel: EELS spectrum along the [100] direction. Right panel: total DOS (solid lines), projected DOS on d-orbital (shaded), and Fermi−Dirac occupation number distribution (dashed lines). Shown are results for $q = 0.0754$ Å^{-1} at ambient conditions [$T = 0.025$ eV], at $T = 2$, $T = 4$, $T = 6$, and at $T = 8$ eV.

Dyson-type equation for the density response function $\chi_{\boldsymbol{G},\boldsymbol{G}'}(\boldsymbol{k}, \omega)$[44,46]

$$\chi_{\boldsymbol{G},\boldsymbol{G}'}(\boldsymbol{k}, \omega) = \chi^0_{\boldsymbol{G},\boldsymbol{G}'}(\boldsymbol{k}, \omega) + \sum_{\boldsymbol{G}_1\boldsymbol{G}_2} \chi^0_{\mathrm{GG}_1}(\boldsymbol{k}, \omega) [v_{\boldsymbol{G}_1}(\boldsymbol{k})\delta_{\boldsymbol{G}_1\boldsymbol{G}_2} + K^{\mathrm{XC}}_{\boldsymbol{G}_1\boldsymbol{G}_2}(\boldsymbol{k}, \omega)]\chi_{\boldsymbol{G}_2\boldsymbol{G}'}(\boldsymbol{k}, \omega) \tag{4}$$

where $v_{\boldsymbol{G}1}(\boldsymbol{k}) = 4\pi/|\boldsymbol{k} + \boldsymbol{G}_1|^2$ is the Coulomb potential in reciprocal space, and $K^{\mathrm{xc}}_{\boldsymbol{G}_1,\boldsymbol{G}_2}(\boldsymbol{k}, \omega)$ is the XC kernel capturing electronic correlations; it is defined as the functional derivative of the XC potential in KS-DFT.[47]

The LR-TDDFT method provides the DSF of the electrons in the thermal equilibrium. An alternative approach that can perform the simulation of electronic dynamics with a distribution different from the Fermi−Dirac distribution is real-time TDDFT (RT-TDDFT), where electronic wave functions are propagated according to time-dependent KS equations. This method was used by Silaeva et al.[48] to study ultrafast electron dynamics thermalization in metals driven by a 7 fs laser pulse. Silaeva et al.[48] showed that valence electrons reach a thermalized state within the time of the laser pulse. The RT-TDDFT method can also be used to compute the DSF. For example, Baczewski et al.[49] used RT-TDDFT to compute the DSF of warm dense beryllium in thermal equilibrium. We note that if the same XC functionals were used in both, RT-TDDFT and LR-TDDFT are formally equivalent for linear response properties in thermal equilibrium.[38]

In our calculations, we have used a static (adiabatic) XC kernel $K^{\mathrm{xc}}_{\boldsymbol{G}_1,\boldsymbol{G}_2}(\boldsymbol{k}, \omega = 0)$ within the ALDA.[38] The ALDA is known to provide a fairly accurate description of the macroscopic dielectric function $\varepsilon_{\mathrm{M}}(\boldsymbol{q},\omega)$ of metals and semiconductors at finite wavenumbers.[22,27,50−52] The relevant thermal signatures explored in this work are characterized by a difference of $\delta\omega \gtrsim 1$ eV from the ground-state features. If needed, a further fine-tuning can be achieved either by employing more advanced static XC kernels beyond ALDA[53,54] or by using an explicitly dynamic approximation (e.g., see ref 46 and references therein) in future works.

We note that, in the ground state, the DSF is usually studied indirectly by measuring the electronic energy loss spectrum (EELS), e.g., see refs 55−57. In principle, the XRTS spectrum and the EELS are directly related since

$$\mathrm{EELS}(\boldsymbol{q}, \omega) = -\mathrm{Im}[\varepsilon^{-1}_{\mathrm{M}}(\boldsymbol{q}, \omega)] \tag{5}$$

From eq 2, one can see that $S(\boldsymbol{q},\omega) \sim q^2\mathrm{EELS}(\boldsymbol{q},\omega)$. This means that EELS is advantageous for measurements at small wavenumbers, whereas XRTS might be more suitable at large wavenumbers. However, EELS measurements are problematic for experiments with matter under extreme conditions due to its requirements for thin targets as well as long measurement times,[57] which are not realistic for the transient states that are of interest in the current work.

In consistency with measurements at FEL facilities, we consider the electronic response on subpicosecond time scales and treat the ions as being frozen in their crystal lattice positions surrounded by heated electrons. This is justified since

https://doi.org/10.1021/acsomega.4c02920
ACS Omega 2024, 9, 25239−25250

the electron−lattice equilibration time is order of picoseconds.[58−63] Furthermore, this approximation is corroborated by the predictions of increased melting temperature with electron heating in copper and other d-band metals[61,64] and by the recent observation of phonon hardening in gold.[17]

2.2. Calculation Parameters. We used the GPAW code,[65−70] which is a real-space implementation of the projector augmented-wave (PAW) approach.[71] We used the ground-state LDA XC functional by Perdew and Wang.[72] The simulations have been carried out for a face-centered cubic (fcc) lattice with the lattice parameter 3.61 Å set according to the experimental value.[73] For the calculation of the KS states, we used the energy cutoff of 1000 eV, the PAW data set of copper provided by GPAW (with 1s−3p orbitals treated as frozen core electrons), and the primitive cell combined with the k-point grid 40 × 40 × 40. We note that in the employed LR-TDDFT formalism, the momentum transfer must be the difference between two k-point times $2\pi/a$. To study the possible impact of inhomogeneity with respect to crystallographic directions on the DSF, calculations were performed along the [100], [111], and [011] directions. We considered electronic temperatures in the range 0.025 eV ≤ T ≤ 12 eV and the number of KS bands was set to N_b = 100. The smearing of the occupation numbers was computed according to the Fermi−Dirac distribution. On the stage of the calculation of the density response matrix, the local field effect cutoff was set to 150 eV. In all calculations, we used η = 0.1 eV for the Lorentzian smearing parameter in $\chi_{\boldsymbol{G},\boldsymbol{G}'}(\boldsymbol{k}, \omega)$.[68] For the density of state (DOS) calculations of copper, we used the same parameters as for the DSF. The DOS was plotted by setting the Gaussian width parameter to 0.2 eV.

3. SIMULATION RESULTS AND DISCUSSION

3.1. DSF $S(q,\omega)$ in the X-ray-Driven Copper. We start our investigation by considering the electronic ground state (here, represented by the results for T = 0.025 eV) in the limit of small wave numbers. In the left panel of Figure 1, we show the EELS spectrum at q = 0.0754 Å^{-1} for different temperatures in the range from 0.025 up to 8 eV (with the temperature increasing in the subplots from the bottom to the top). We focus on four main features of the EELS spectrum (which equivalently appear in the DSF, cf. Figure 4) denoted by capital letters A−D. A thorough investigation of the EELS properties of copper in the ground state has been presented by Alkauskas et al.,[28] where it was shown that features A and B are plasmon-type collective oscillations, whereas C and D are a consequence of excitations between the d-band and the unoccupied states above the Fermi level. More specifically, peak B can be described as a collective plasmon oscillation of the valence electrons; this has been shown by Campillo et al.[29] by freezing the d-band into the core and leaving only the 4s^1 state that forms the valence electron. Our LR-TDDFT results are in good agreement with the structure of electronic excitations reported in refs 28 and 29 and we reproduce the positions of all four peaks A−D.

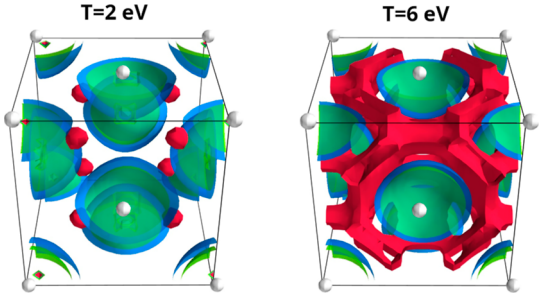

Figure 2. Electronic density accumulation in the interstitial region and density depletion around the ions due to heating at T = 2 eV (left) and T = 6 eV (right). The surface plots (semitransparent) indicate the density change with respect to the ground state, $\delta n(\boldsymbol{r}) = n_T(\boldsymbol{r}) - n_0(\boldsymbol{r})$, i.e., relative to the density at T = 0.025 eV. The blue surface corresponds to $\delta n(\boldsymbol{r})$ = 0, the red surface indicates $\delta n(\boldsymbol{r}) = \max[\delta n(\boldsymbol{r})]/70 > 0$, and the green surface indicates $\delta n(\boldsymbol{r}) = \min[\delta n(\boldsymbol{r})]/15 < 0$.

Let us next turn to the central topic of this work, which is the study of the impact of thermal effects. With increasing temperature, the positions of peaks B, C, and D shift to larger energies. Moreover, the amplitude of the plasmon feature B gets substantially amplified. In contrast, the signature of feature A nearly vanishes for $T \geq 2$ eV. Compared to peaks A and B, the magnitude of features C and D is only weakly affected by heating.

Following the analysis by Campillo et al.,[29] who investigated the DSF of copper at ambient conditions, signatures B and C can be understood by considering the DOS, which is shown in the right panel of Figure 1 as the solid lines. The d-band dominates the accumulation of the states below the Fermi energy. This is shown by the projected DOS on d-states, which is depicted by the shaded area. We find that, with increasing temperatures, the d-states are shifted to lower energies. Since the features C and D in the EELS/DSF emerge as the result of the transitions from d-states to high-lying bands above the Fermi level, the observed shift of the d-states results in a blue shift by approximately the same amount. An accurate determination of the difference in the shifts of the C and D peaks is difficult due to the strong broadening of the C peak. Nevertheless, one can observe that the blue shift of C and D peaks has close values at T < 4 eV. We estimate that the D peak of the EELS shifts by about 1 eV more toward larger frequencies at T = 8 and T = 6 eV compared to the C peak.

In addition, increasing the temperature leads to an increased number of conduction electrons, which, in turn, leads to a larger plasmon frequency, i.e., a substantial blue shift of feature B. The corresponding increase in the electronic density in the interstitial region between the fixed ions can be demonstrated by investigating the change in the electronic density $\delta n(\boldsymbol{r})$ with respect to the ground state. For T = 2 eV (T = 6 eV), in atomic units, we find $\max[\delta n(\boldsymbol{r})] \simeq 1.45$ ($\max[\delta n(\boldsymbol{r})] \simeq 3.974$) and $\min[\delta n(\boldsymbol{r})] \simeq -0.375$ ($\min[\delta n(\boldsymbol{r})] \simeq -0.966$). This is illustrated in more detail in Figure 2, where we show the thermally induced density change in the 3D simulation box for both temperatures. The blue surface depicts $\delta n(\boldsymbol{r})$ = 0; the red surface indicates $\delta n(\boldsymbol{r}) > 0$ (for the illustration, we choose $\delta n(\boldsymbol{r}) = \max[\delta n(\boldsymbol{r})]/70$); and the green surface indicates $\delta n(\boldsymbol{r}) < 0$ (here, we show $\delta n(\boldsymbol{r}) = \min[\delta n(\boldsymbol{r})]/15$). We can thus clearly see that the electronic density is reduced in the vicinity of the ions and accumulates in the interstitial region, which is more pronounced for the higher temperature, as it is expected. A more detailed, quantitative analysis of the increased free-electronic density and the resulting plasmon blue shift is presented in Section 3.2 below.

Let us next investigate the DSF, which is the key property in XRTS experiments; it is shown in Figure 3 along the [100] direction for 0.0754 Å$^{-1} \leq q \leq$ 1.4794 Å^{-1}. Since feature A is strongly damped for $T \geq 2$ eV, we will ignore it in the

https://doi.org/10.1021/acsomega.4c02920
ACS Omega 2024, 9, 25239−25250

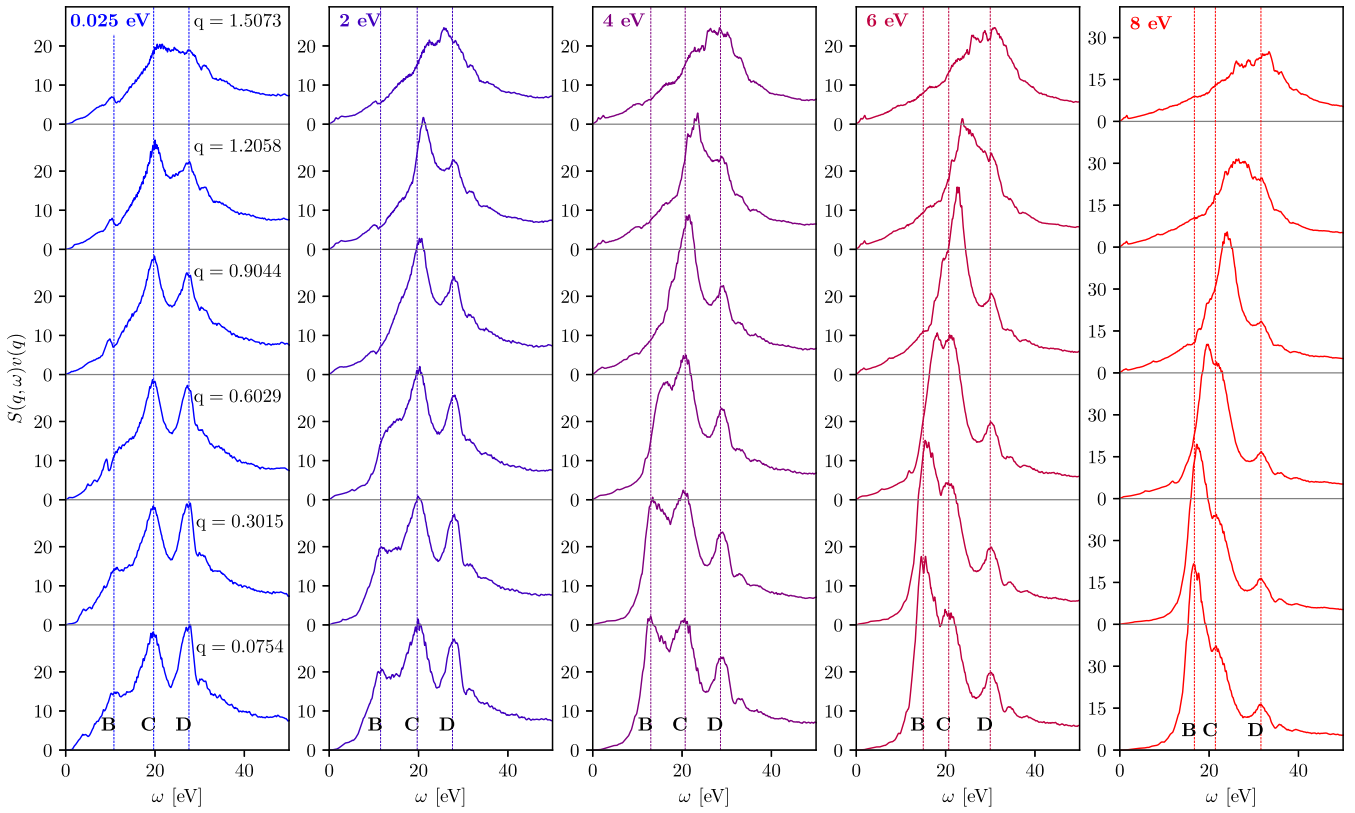

Figure 3. LR-TDDFT results for the DSF of fcc Cu along the [100] direction at different wavenumbers for the ground state with T = 0.025 eV and for isochorically heated electrons with T = 2, T = 4, T = 6, and T = 8 eV. The wavenumber values are given in the units of Å^{-1}.

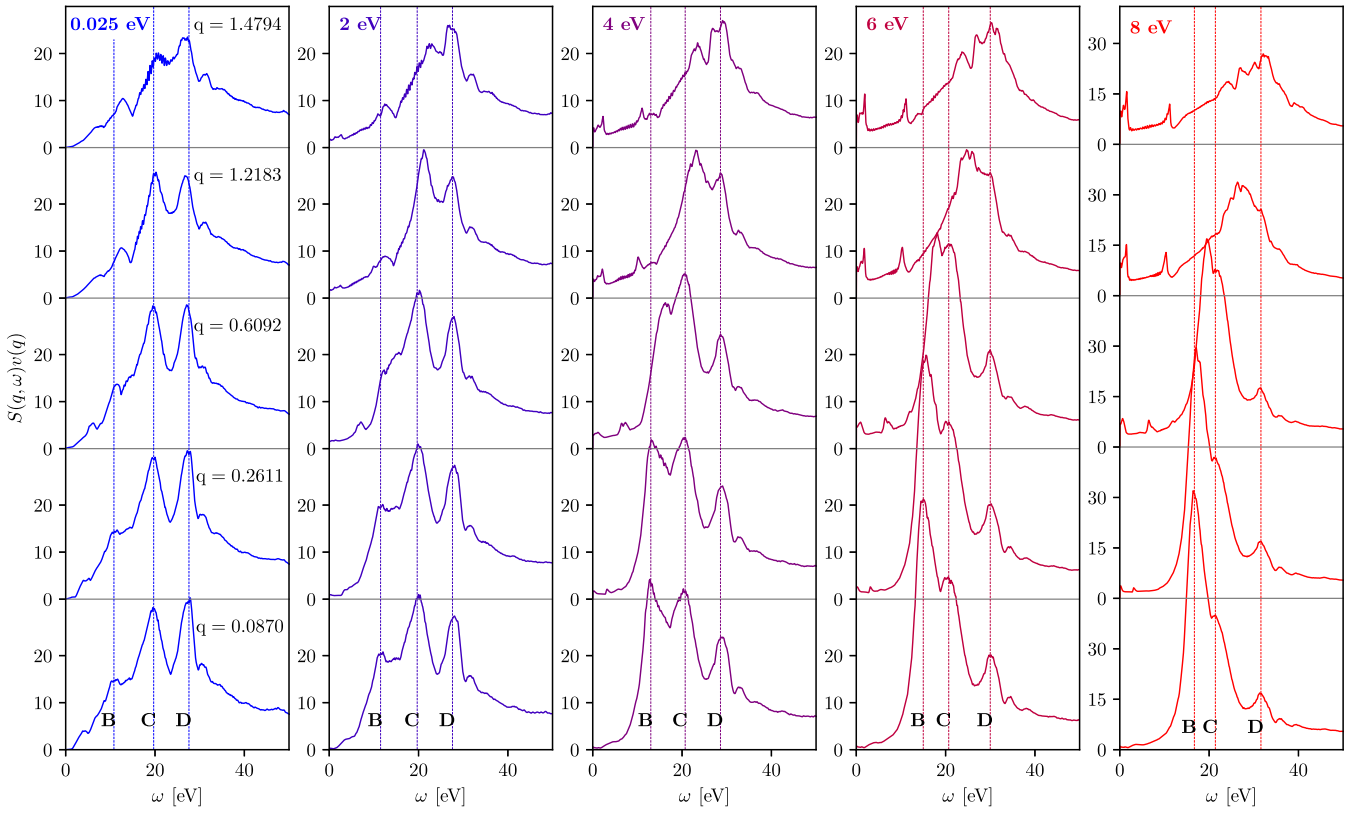

Figure 4. LR-TDDFT results for the DSF of fcc Cu along the [011] direction at different wavenumbers for the ground state with T = 0.025 eV and for heated electrons with T = 2, T = 4, T = 6, and T = 8 eV. The wavenumber values are given in the units of Å^{-1}.

https://doi.org/10.1021/acsomega.4c02920
ACS Omega 2024, 9, 25239−25250

following discussion and instead focus on the thermally induced changes of features B, C, and D. At all considered temperatures, the position of features C and D is nearly independent of the wavenumber. In stark contrast, the plasmon feature B exhibits a considerably richer behavior. At $T = 0.025$ and at $T = 2$ eV, its position does not follow the Bohm−Gross-type dispersion of the free-electron gas.[40] Overall, it is difficult to quantify its q-dependence for these two temperatures due to the comparably weak spectral weight and the possible overlap with other features due to local field effects created by the lattice structure.[28] In contrast, we observe a pronounced increase with q for $T \geq 4$ eV. As a result, the plasmon eventually overtakes feature C, leading to the disappearance of the latter from the DSF at $q \gtrsim 0.9$ Å^{-1} in the cases of $T = 4$ and $T = 6$ eV and at $q \gtrsim 0.6$ Å^{-1} for $T = 8$ eV.

An additional interesting research topic is due to the lattice structure, which is known to lead to an anisotropy of the DSF with respect to the crystallographic direction at certain wavenumbers.[28,56] To quantify this anisotropy effect on X-ray-driven copper, we show the DSF in the [011] direction at different temperatures and wavenumbers in Figure 4. We find that the DSF in the [011] direction closely resembles the DSF in the [100] direction for $q \lesssim 0.9$ Å^{-1}, and differences in the shape and peak positions emerge for $q \gtrsim 1.2$ Å^{-1}. For completeness, we note that the DSF in [111] direction is equivalent to the [100] direction (see the Appendix). In summary, we conclude that the electronic DSF of copper is nearly isotropic at $T \geq 2$ eV for $q \lesssim 0.9$ Å^{-1}.

In addition to the discussed dominant features, we observe an increase in the DSF at low energies and a new peaked feature emerges in the DSF at $\omega < 10$ eV in both [100] and [011] directions at $T \geq 4$ eV and $q \gtrsim 0.6$ Å^{-1}. The increase in the temperature modifies the DSF due to the factor $f(\omega)=(1 - e^{-\hbar\omega/k_BT})^{-1}$ in eq 2. This effect is particularly pronounced for the low-energy part of the DSF and enhances subtle features in this regime. This is illustrated in Figure 5 for $T = 4$ and $T = 6$ eV at wavenumbers $q = 0.9044$, $q = 1.2058$, and $q = 1.5073$ Å^{-1}. From Figure 5, we observe that the factor $f(\omega)$ in eq 2 for the DSF results in the substantial increase of the DSF values at low energies leading to an amplification of the thermally induced features at $\omega < 10$ eV. Physically, these features might originate from transitions between accumulated states located closely above the Fermi level, cf. Figure 1. Indeed, one can observe that at $T \geq 4$ eV, states above the Fermi level become partially occupied allowing the emergence of new excitation features.

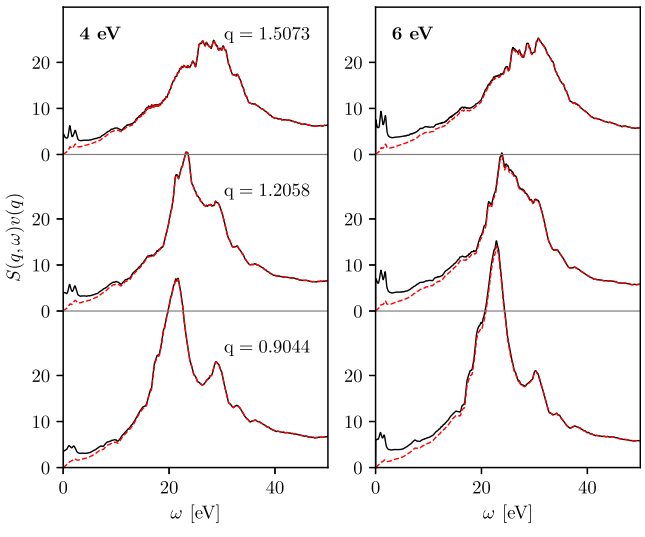

Figure 5. Demonstration of the role of the factor $f(\omega)=(1 - e^{-\hbar\omega/k_BT})^{-1}$ on the enhancement of the DSF features at small energies. Solid lines are the results for the DSF along the [100] direction and dashed lines are the same data divided by $f(\omega)$. The wavenumber values are given in the units of Å^{-1}.

3.2. Plasmon Dispersion and Conditions in Interstitial Regions. Analyzing the DSF, we have found that the collective plasmon oscillations in X-ray-driven copper overcome the dominance of the d-band excitations, eventually overtaking them with respect to the spectral weight. In addition, the plasmon position starts to exhibit a substantial dispersion with respect to the wavenumber for sufficiently high temperatures, which is in contrast to the ground-state plasmon. To examine the character of the plasmon dispersion, we show the dependence of the plasmon energy (frequency) on the wavenumber, $\omega(q)$, in Figure 6 for different temperatures.

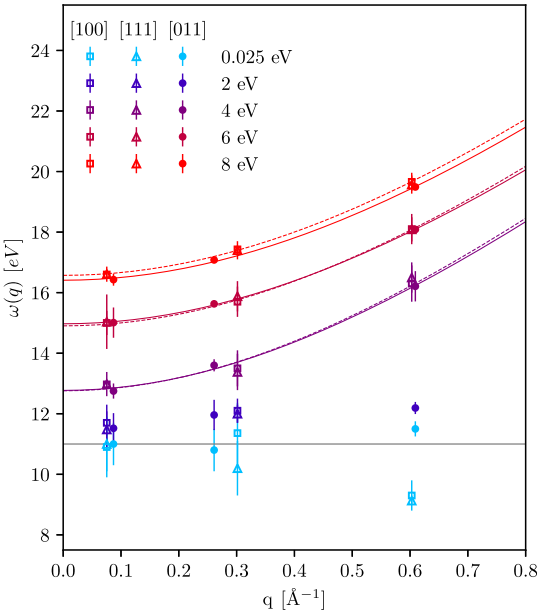

Figure 6. Dependence of the plasmon frequency on the wavenumber along different crystallographic directions at $T = 0.025$, $T = 2$, $T = 4$, $T = 6$, and $T = 8$ eV. Solid (dashed) lines show Bohm−Gross-type quadratic dispersion fits [cf. eq 6] for the direction [111] ([100]) at $T = 4$, $T = 6$, and $T = 8$ eV. In Bohm−Gross dispersion (6), we used for [111] ([100]) $\alpha = 1.66\omega_p^2$ ($\alpha = 1.7\omega_p^2$) at $T = 4$ eV, $\alpha = 1.24\omega_p^2$ ($\alpha = 1.3\omega_p^2$) at $T = 6$ eV, and $\alpha = 1.11\omega_p^2$ ($\alpha = 1.25\omega_p^2$) at $T = 8$ eV. The horizontal solid gray line at 10.864 eV indicates the plasmon energy computed using the free-electron gas model, i.e., assigning the 3d shell as a core state [e.g., see ref 29].

We consider $q < 1$ Å^{-1}, where the plasmon peak can be clearly identified at all considered temperatures and independent of the crystallographic direction. The uncertainty in the plasmon position is evaluated by looking at the onset of a broadened peak. At $T = 2$ eV, we find that $\omega(q)$ is qualitatively similar to the results for $T = 0.025$ eV. For $T \geq 4$ eV, the plasmon dispersion starts to follow the familiar quadratic dependence on q that is well known from the free-electron gas model.[74] To further quantify this trend, we fit the LR-TDDFT results using the Bohm−Gross-type dispersion relation[75,76]

https://doi.org/10.1021/acsomega.4c02920
ACS Omega 2024, 9, 25239−25250

Table 1. Plasmon Energy at $q = 0.0754$ Å^{-1} Extracted from the DSF Calculations with Corresponding Effective Density Parameter $\tilde{r}_s$, Effective Degeneracy Parameter $\tilde{\Theta}$, and Effective Charge of Ions $\tilde{Z}$

T [eV]	ω_p [eV]	$\tilde{r}_s$	$\tilde{\Theta}$	$\tilde{Z}$
0.025	11 ± 0.7	2.64 ± 0.11	0	1.0 ± 0.06
2	11.52 ± 0.5	2.56 ± 0.07	0.261 ± 0.01	1.1 ± 0.09
4	12.75 ± 0.25	2.39 ± 0.03	0.456 ± 0.01	1.34 ± 0.14
6	15.01 ± 0.5	2.14 ± 0.04	0.551 ± 0.02	1.86 ± 0.17
8	16.43 ± 0.2	2.02 ± 0.02	0.651 ± 0.01	2.23 ± 0.25
10	18.3 ± 0.4	1.88 ± 0.027	0.704 ± 0.02	2.77 ± 0.29
12	19.43 ± 0.35	1.80 ± 0.02	0.780 ± 0.019	3.12 ± 0.33

$$\omega^2(q) = \omega_p^2 + \alpha q^2 \tag{6}$$

where α and ω_p are the free parameters. The results are shown as the solid ([011] direction) and dashed ([100] direction) lines in Figure 6, which are nearly identical; the small differences are likely due to uncertainties introduced by the broadened peaks of the DSF.

In Section 3.1, we have indicated that the increase in the plasmon energy with the temperature is a consequence of the excess electronic density in the interstitial regions between the ionic lattice, cf. Figure 2. Here, we propose to utilize such forward scattering data for the DSF as a diagnostic for the free-electronic density and for the effective charge state. Specifically, we define the effective density parameter $\tilde{r}_s$ by inverting the usual relation between the density and the plasmon frequency of a free-electron gas

$$\omega_\mathrm{p} = \left(4\pi\tilde{n}\frac{e^2}{m_\mathrm{e}}\right)^{1/2} \Rightarrow \tilde{r}_\mathrm{s} = \left(\frac{3}{4\pi}\tilde{n}\right)^{1/3} \tag{7}$$

We note that the parameter $\tilde{r}_\mathrm{s}$ also characterizes the coupling strength or, equivalently, the degree of nonideality of the free electrons.[31,77]

An additional, related effective parameter of interest is given by the corresponding degeneracy temperature $\tilde{\Theta} = k_\mathrm{B}T/E_\mathrm{F}(\tilde{n})$, where $E_\mathrm{F}(\tilde{n}) = (3\pi^2\tilde{n})^{1/3}$ denotes the Fermi energy of a free-electron gas of density $\tilde{n}$.[40] Finally, we consider the effective ionic charge $\tilde{Z}$, which is a key ingredient to equation-of-state tables.[9,10] The effective charge is computed using $\tilde{Z} = (\tilde{r}_s(T=0)/\tilde{r}_s(T))^3$, which follows from the condition $\tilde{Z}n_\mathrm{i} = \tilde{n}$, with n_i = constant being the number density of ions, and setting $Z = 1$ for copper at $T = 0$ since we have one valence electron in the 4s state.

In Table 1, we provide an overview of these parameters for all selected temperatures. For $T = 0.025$ eV, we find an effective density parameter of $\tilde{r}_s = 2.64 \pm 0.11$, which agrees with the value $r_\mathrm{s} = 2.668$ that corresponds to the conduction electron density in the fcc copper at room temperature.

Upon increasing the temperature, we find a monotonic increase in the density of effectively free electrons, leading to a corresponding decrease of $\tilde{r}_s$ and an increase in $\tilde{Z}$. The observed monotonic increase of $\tilde{\Theta}$ is less trivial. On the one hand, we have $\tilde{\Theta} \sim \tilde{r}_s^2$,[77] which, by itself, would indicate a decrease of $\tilde{\Theta}$ with T. However, this effect is overridden by the relation $\tilde{\Theta} \sim T$ in practice.

Table 1 clearly shows that the effectively free electrons in the interstitial region of isochorically heated copper are in the WDM regime.[30] In nature, WDM occurs in a variety of astrophysical objects such as giant planet interiors,[3] brown dwarfs,[34] and white dwarf atmospheres.[33] In the laboratory, these conditions are encountered on the compression path of a fuel capsule and its ablator in inertial confinement fusion experiments,[4,6,36] and, in addition, they are relevant for material science, synthesis, and discovery.[78,79] Despite its fundamental importance for a gamut of applications, the rigorous theoretical description of WDM remains challenging: it must cover the complex interplay between effects such as partial ionization, Coulomb coupling, and quantum degeneracy and diffraction, which is notoriously difficult in practice.[30−32] Our new simulation results thus imply that future XRTS experiments with isochorically heated copper constitute a suitable and highly controlled testbed for the benchmarking of theoretical methods and simulations.

4. CONCLUSIONS

Motivated by experimental capabilities at modern FEL facilities, we have performed a detailed study of the changes in the electronic DSF in fcc copper due to isochoric heating. Our new LR-TDDFT simulations show that the heating induces a prominent plasmon feature that eventually becomes dominant over the d-band signal. This is in marked contrast to the ground state, where the plasmon is strongly damped by the presence of d-band excitations, and where it does not exhibit a meaningful dispersion with respect to the wavenumber q. Indeed, we have shown that at $T \geq 4$ eV, the plasmon dispersion follows the familiar Bohm−Gross-type relation, and the plasma frequency ω_p substantially increases with the temperature. This has been explained by the accumulation of effectively free electrons in the interstitial region between the ions. This, in turn, is a consequence of the availability of the electrons in the d-orbitals for filling states in the quasicontinuum when the temperature is increased. Interestingly, the reported behavior of the plasmon in copper is fundamentally different from isochorically heated aluminum (Al), where LR-TDDFT simulations have shown that heating to a few electronvolts (at $T \lesssim 7$ eV) causes a red shift of ω_p.[23] In this regard, we note that Al has 3 valence electrons from 3p3s orbitals and further ionization of the electrons from 2p requires temperatures about 70 eV. Therefore, in contrast to copper, thermal excitations in Al are not accompanied by an increase in the density of valence electrons with the increase in the temperature at $T \lesssim 10$ eV.

From a physical perspective, we find that the quasi-free electrons in the interstitial space are in the WDM regime with an effective density parameter $\tilde{r}_s \sim 2$ and an effective degeneracy temperature $\tilde{\Theta} \sim 0.5$. In addition to being interesting in their own right, such extreme conditions occur in a wealth of astrophysical objects and play a key role in experiments with inertial confinement fusion and material

https://doi.org/10.1021/acsomega.4c02920
ACS Omega 2024, 9, 25239−25250

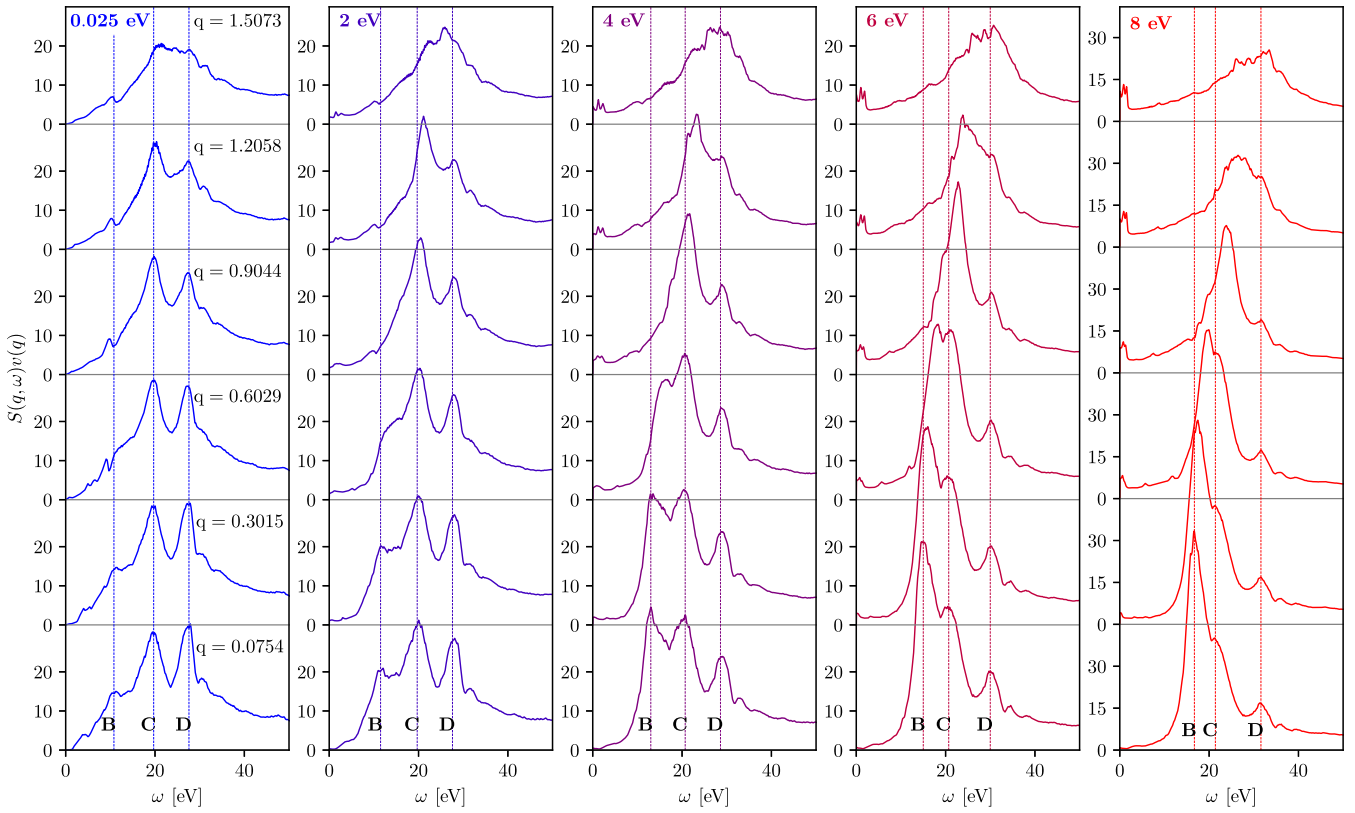

Figure 7. LR-TDDFT results for the DSF of fcc Cu along the [111] direction at different wavenumbers for the ground state with T = 0.025 eV and for heated electrons with T = 2, T = 4, T = 6, and T = 8 eV. The wavenumber values are given in the units of Å^{-1}.

science. In practice, there does not exist a single method that is capable of giving an accurate description of WDM states over the entire relevant parameter space, and the interpretation, modeling, and design of corresponding experiments are usually based on a number of defacto uncontrolled approximations.

In this regard, we propose to use future XRTS experiments with isochorically heated copper as a controlled testbed for the rigorous assessment of different theoretical models and simulation tools for the description of WDM. Ideally, one might infer the temperature of the heated sample based on the model-free imaginary-time thermometry approach[11,12] as a first step. Indeed, even the inference of comparably moderate temperatures of $T \sim 1-10$ eV is expected to be feasible using the new high-resolution setup that has recently been demonstrated at the European XFEL in Germany.[22] Second, we propose to carry out measurements at multiple scattering angles (i.e., multiple wavenumbers q) to observe the plasmon dispersion $\omega(q)$ and, in this way, to infer the effective charge state $\tilde{Z}$ and the effective density parameter $\tilde{r}_s$. Since the ambient density is a-priori known, this will give one full access to the most relevant parameters of the system. This is an important advantage over shock experiments, or XRTS measurements with backlighter sources,[37] where one or multiple of these parameters can only be inferred on the basis of the theoretical models which we aim to test in the first place. Isochoric heating can be achieved by employing a 400 nm optical short-pulse laser on thin targets and combining it with the delayed FEL probe.[80,81] Alternatively, one can use X-ray pump and X-ray probe beams that are separated in both color and time. Proper time separation allows heating to be completed by the pump before the target is probed. Such X-ray pump and X-ray probe experiments can be performed at European XFEL[82] and at SACLA in Japan.[83,84] A detailed discussion of the feasibility of measuring thermal excitations in the DSF of isochorically heated targets is provided in ref 23.

Such a hypothetical XRTS data set can then be used to benchmark the zoo of available theoretical methods such as the widely used effective chemical models.[19,85,86] A particularly interesting question is the assessment of XC functionals in KS-DFT simulations, including the resolution of explicitly thermal XC effects.[87−92] Moreover, frequency-resolved inelastic X-ray scattering data for a set of finite wavenumbers q will be ideally suited to gauge the accuracy of different XC kernels in LR-TDDFT calculations, including a rigorous assessment of the popular adiabatic approximation.[38,42,93] As a WDM testbed, the observed isotropy of the DSF of electrons in copper is advantageous for achieving unambiguous conclusions in the assessment of various models.

APPENDIX

For completeness, we show the DSF in the [111] direction at the different considered temperatures and wavenumbers in Figure 7. We find that the B, C, and D features behave similarly to our results for the [100] and [111] directions, both with respect to temperature and wavenumber. Indeed, the DSF in the [111] direction is nearly identical to the DSF in [100] direction over the entire depicted q-range.

AUTHOR INFORMATION

Corresponding Author

Zhandos Moldabekov − *Center for Advanced Systems Understanding (CASUS), D-02826 Görlitz, Germany; Helmholtz-Zentrum Dresden-Rossendorf (HZDR), D-01328*

https://doi.org/10.1021/acsomega.4c02920
ACS Omega 2024, 9, 25239−25250

Dresden, Germany; orcid.org/0000-0002-9725-9208; Email: z.moldabekov@hzdr.de

Authors

Thomas D. Gawne − *Center for Advanced Systems Understanding (CASUS), D-02826 Görlitz, Germany; Helmholtz-Zentrum Dresden-Rossendorf (HZDR), D-01328 Dresden, Germany*

Sebastian Schwalbe − *Center for Advanced Systems Understanding (CASUS), D-02826 Görlitz, Germany; Helmholtz-Zentrum Dresden-Rossendorf (HZDR), D-01328 Dresden, Germany*

Thomas R. Preston − *European XFEL, D-22869 Schenefeld, Germany*

Jan Vorberger − *Helmholtz-Zentrum Dresden-Rossendorf (HZDR), D-01328 Dresden, Germany*

Tobias Dornheim − *Center for Advanced Systems Understanding (CASUS), D-02826 Görlitz, Germany; Helmholtz-Zentrum Dresden-Rossendorf (HZDR), D-01328 Dresden, Germany;* orcid.org/0000-0001-7293-6615

Complete contact information is available at: https://pubs.acs.org/10.1021/acsomega.4c02920

Notes

The authors declare no competing financial interest.

■ ACKNOWLEDGMENTS

This work was partially supported by the Center for Advanced Systems Understanding (CASUS), financed by Germany's Federal Ministry of Education and Research (BMBF), and the Saxon state government out of the State budget approved by the Saxon State Parliament. This work has received funding from the European Union's Just Transition Fund (JTF) within the project Röntgenlaser-Optimierung der Laserfusion (ROLF), contract no. 5086999001, cofinanced by the Saxon state government out of the State budget approved by the Saxon State Parliament. This work has received funding from the European Research Council (ERC) under the European Union's Horizon 2022 research and innovation programme (grant agreement no. 101076233, "PREXTREME"). Views and opinions expressed are however those of the authors only and do not necessarily reflect those of the European Union or the European Research Council Executive Agency. Neither the European Union nor the granting authority can be held responsible for them. Computations were performed on a Bull Cluster at the Center for Information Services and High-Performance Computing (ZIH) at Technische Universität Dresden, at the Norddeutscher Verbund für Hoch-und Höchstleistungsrechnen (HLRN) under grant mvp00024, and on the HoreKa supercomputer funded by the Ministry of Science, Research and the Arts Baden-Württemberg, and by the Federal Ministry of Education and Research.

■ REFERENCES

(1) Millot, M.; Hamel, S.; Rygg, J. R.; Celliers, P. M.; Collins, G. W.; Coppari, F.; Fratanduono, D. E.; Jeanloz, R.; Swift, D. C.; Eggert, J. H. Experimental evidence for superionic water ice using shock compression. *Nat. Phys.* **2018**, *14*, 297−302.

(2) Morales, M. A.; Pierleoni, C.; Schwegler, E.; Ceperley, D. M. Evidence for a first-order liquid-liquid transition in high-pressure hydrogen from ab initio simulations. *Proc. Natl. Acad. Sci. U.S.A.* **2010**, *107*, 12799−12803.

(3) Benuzzi-Mounaix, A.; Mazevet, S.; Ravasio, A.; Vinci, T.; Denoeud, A.; Koenig, M.; Amadou, N.; Brambrink, E.; Festa, F.; Levy, A.; Harmand, M.; Brygoo, S.; Huser, G.; Recoules, V.; Bouchet, J.; Morard, G.; Guyot, F.; Resseguier, T. d.; Myanishi, K.; Ozaki, N.; Dorchies, F.; Gaudin, J.; Leguay, P. M.; Peyrusse, O.; Henry, O.; Raffestin, D.; Pape, S. L.; Smith, R.; Musella, R. Progress in warm dense matter study with applications to planetology. *Phys. Scr.* **2014**, *T161*, 014060.

(4) Hu, S. X.; Militzer, B.; Goncharov, V. N.; Skupsky, S. First-principles equation-of-state table of deuterium for inertial confinement fusion applications. *Phys. Rev. B: Condens. Matter Mater. Phys.* **2011**, *84*, 224109.

(5) Fernandez-Pañella, A.; Millot, M.; Fratanduono, D. E.; Desjarlais, M. P.; Hamel, S.; Marshall, M. C.; Erskine, D. J.; Sterne, P. A.; Haan, S.; Boehly, T. R.; Collins, G. W.; Eggert, J. H.; Celliers, P. M. Shock Compression of Liquid Deuterium up to 1 TPa. *Phys. Rev. Lett.* **2019**, *122*, 255702.

(6) Betti, R. A milestone in fusion research is reached. *Nat. Rev. Phys.* **2022**, *5*, 6−8.

(7) Miao, M.; Sun, Y.; Zurek, E.; Lin, H. Chemistry under high pressure. *Nat. Rev. Chem* **2020**, *4*, 508−527.

(8) Regan, S. P.; Falk, K.; Gregori, G.; Radha, P. B.; Hu, S. X.; Boehly, T. R.; Crowley, B. J. B.; Glenzer, S. H.; Landen, O. L.; Gericke, D. O.; Döppner, T.; Meyerhofer, D. D.; Murphy, C. D.; Sangster, T. C.; Vorberger, J. Inelastic X-Ray Scattering from Shocked Liquid Deuterium. *Phys. Rev. Lett.* **2012**, *109*, 265003.

(9) Falk, K.; Gamboa, E. J.; Kagan, G.; Montgomery, D. S.; Srinivasan, B.; Tzeferacos, P.; Benage, J. F. Equation of State Measurements of Warm Dense Carbon Using Laser-Driven Shock and Release Technique. *Phys. Rev. Lett.* **2014**, *112*, 155003.

(10) Döppner, T.; Bethkenhagen, M.; Kraus, D.; Neumayer, P.; Chapman, D. A.; Bachmann, B.; Baggott, R. A.; Böhme, M. P.; Divol, L.; Falcone, R. W.; Fletcher, L. B.; Landen, O. L.; MacDonald, M. J.; Saunders, A. M.; Schörner, M.; Sterne, P. A.; Vorberger, J.; Witte, B. B. L.; Yi, A.; Redmer, R.; Glenzer, S. H.; Gericke, D. O. Observing the onset of pressure-driven K-shell delocalization. *Nature* **2023**, *618*, 270−275.

(11) Dornheim, T.; Böhme, M.; Kraus, D.; Döppner, T.; Preston, T. R.; Moldabekov, Z. A.; Vorberger, J. Accurate temperature diagnostics for matter under extreme conditions. *Nat. Commun.* **2022**, *13*, 7911.

(12) Dornheim, T.; Böhme, M. P.; Chapman, D. A.; Kraus, D.; Preston, T. R.; Moldabekov, Z. A.; Schlünzen, N.; Cangi, A.; Döppner, T.; Vorberger, J. Imaginary-time correlation function thermometry: A new, high-accuracy and model-free temperature analysis technique for x-ray Thomson scattering data. *Phys. Plasmas* **2023**, *30*, 042707.

(13) Dornheim, T.; Döppner, T.; Tolias, P.; Böhme, M.; Fletcher, L.; Gawne, T.; Graziani, F.; Kraus, D.; MacDonald, M.; Moldabekov, Z.; Schwalbe, S.; Gericke, D.; Vorberger, J. Unraveling electronic correlations in warm dense quantum plasmas. *arXiv* **2024**, arXiv:2402.19113.

(14) Zastrau, U.; Appel, K.; Baehtz, C.; Baehr, O.; Batchelor, L.; Berghäuser, A.; Banjafar, M.; Brambrink, E.; Cerantola, V.; Cowan, T. E.; Damker, H.; Dietrich, S.; Di Dio Cafiso, S.; Dreyer, J.; Engel, H.-O.; Feldmann, T.; Findeisen, S.; Foese, M.; Fulla-Marsa, D.; Göde, S.; Hassan, M.; Hauser, J.; Herrmannsdörfer, T.; Höppner, H.; Kaa, J.; Kaever, P.; Knöfel, K.; Konôpková, Z.; Laso García, A.; Liermann, H.-P.; Mainberger, J.; Makita, M.; Martens, E.-C.; McBride, E. E.; Möller, D.; Nakatsutsumi, M.; Pelka, A.; Plueckthun, C.; Prescher, C.; Preston, T. R.; Röper, M.; Schmidt, A.; Seidel, W.; Schwinkendorf, J.-P.; Schoelmerich, M. O.; Schramm, U.; Schropp, A.; Strohm, C.; Sukharnikov, K.; Talkovski, P.; Thorpe, I.; Toncian, M.; Toncian, T.; Wollenweber, L.; Yamamoto, S.; Tschentscher, T. The High Energy Density Scientific Instrument at the European XFEL. *J. Synchrotron Radiat.* **2021**, *28*, 1393−1416.

(15) Fletcher, L. B.; Lee, H. J.; Döppner, T.; Galtier, E.; Nagler, B.; Heimann, P.; Fortmann, C.; LePape, S.; Ma, T.; Millot, M.; Pak, A.; Turnbull, D.; Chapman, D. A.; Gericke, D. O.; Vorberger, J.; White, T.; Gregori, G.; Wei, M.; Barbrel, B.; Falcone, R. W.; Kao, C.-C.;

Nuhn, H.; Welch, J.; Zastrau, U.; Neumayer, P.; Hastings, J. B.; Glenzer, S. H. Ultrabright X-ray laser scattering for dynamic warm dense matter physics. *Nat. Photonics* **2015**, *9*, 274−279.
(16) Vorberger, J.; Preston, T. R.; Medvedev, N.; Böhme, M. P.; Moldabekov, Z. A.; Kraus, D.; Dornheim, T. Revealing non-equilibrium and relaxation in laser heated matter. *Phys. Lett. A* **2024**, *499*, 129362.
(17) Descamps, A.; Ofori-Okai, B. K.; Bistoni, O.; Chen, Z.; Cunningham, E.; Fletcher, L. B.; Hartley, N. J.; Hastings, J. B.; Khaghani, D.; Mo, M.; Nagler, B.; Recoules, V.; Redmer, R.; Schörner, M.; Senesky, D. G.; Sun, P.; Tsai, H.-E.; White, T. G.; Glenzer, S. H.; McBride, E. E. Evidence for phonon hardening in laser-excited gold using x-ray diffraction at a hard x-ray free electron laser. *Sci. Adv.* **2024**, *10*, No. eadh5272.
(18) Descamps, A.; Ofori-Okai, B. K.; Appel, K.; Cerantola, V.; Comley, A.; Eggert, J. H.; Fletcher, L. B.; Gericke, D. O.; Goede, S.; Humphries, O.; Karnbach, O.; Lazicki, A.; Loetzsch, R.; McGonegle, D.; Palmer, C. A. J.; Plueckthun, C.; Preston, T. R.; Redmer, R.; Senesky, D. G.; Strohm, C.; Uschmann, I.; White, T. G.; Wollenweber, L.; Monaco, G.; Wark, J. S.; Hastings, J. B.; Zastrau, U.; Gregori, G.; Glenzer, S. H.; McBride, E. E. An approach for the measurement of the bulk temperature of single crystal diamond using an X-ray free electron laser. *Sci. Rep.* **2020**, *10*, 14564.
(19) Glenzer, S. H.; Redmer, R. X-ray Thomson scattering in high energy density plasmas. *Rev. Mod. Phys.* **2009**, *81*, 1625−1663.
(20) Biswas, R.; Ambegaokar, V. Phonon spectrum of a model of electronically excited silicon. *Phys. Rev. B: Condens. Matter Mater. Phys.* **1982**, *26*, 1980−1988.
(21) Mo, C.; Fu, Z.; Kang, W.; Zhang, P.; He, X. T. First-Principles Estimation of Electronic Temperature from X-Ray Thomson Scattering Spectrum of Isochorically Heated Warm Dense Matter. *Phys. Rev. Lett.* **2018**, *120*, 205002.
(22) Gawne, T.; Moldabekov, Z. A.; Humphries, O. S.; Appel, K.; Bähtz, C.; Bouffetier, V.; Brambrink, E.; Cangi, A.; Göde, S.; Konôpková, Z.; Makita, M.; Mishchenko, M.; Nakatsutsumi, M.; Ramakrishna, K.; Randolph, L.; Schwalbe, S.; Vorberger, J.; Wollenweber, L.; Zastrau, U.; Dornheim, T.; Preston, T. R. Ultrahigh Resolution X-ray Thomson Scattering Measurements of Electronic Structures. *arXiv* **2024**, arXiv:2403.02776.
(23) Moldabekov, Z. A.; Gawne, T. D.; Schwalbe, S.; Preston, T. R.; Vorberger, J.; Dornheim, T. Excitation signatures of isochorically heated electrons in solids at finite wavenumber explored from first principles. *arXiv* **2024**, arXiv:2402.09005.
(24) Wollenweber, L.; Preston, T. R.; Descamps, A.; Cerantola, V.; Comley, A.; Eggert, J. H.; Fletcher, L. B.; Geloni, G.; Gericke, D. O.; Glenzer, S. H.; Göde, S.; Hastings, J.; Humphries, O. S.; Jenei, A.; Karnbach, O.; Konopkova, Z.; Loetzsch, R.; Marx-Glowna, B.; McBride, E. E.; McGonegle, D.; Monaco, G.; Ofori-Okai, B. K.; Palmer, C. A. J.; Plückthun, C.; Redmer, R.; Strohm, C.; Thorpe, I.; Tschentscher, T.; Uschmann, I.; Wark, J. S.; White, T. G.; Appel, K.; Gregori, G.; Zastrau, U. High-resolution inelastic x-ray scattering at the high energy density scientific instrument at the European X-Ray Free-Electron Laser. *Rev. Sci. Instrum.* **2021**, *92*, 013101.
(25) Schülke, W.; Schulte-Schrepping, H.; Schmitz, J. R. Dynamic structure of electrons in Al metal studied by inelastic x-ray scattering. *Phys. Rev. B: Condens. Matter Mater. Phys.* **1993**, *47*, 12426−12436.
(26) Larson, B.; Tischler, J.; Fleszar, A.; Eguiluz, A. Correlation and band structure effects in the electronic energy loss spectra of Al: an experimental perspective. *J. Phys. Chem. Solids* **2000**, *61*, 391−396.
(27) Cazzaniga, M.; Weissker, H.-C.; Huotari, S.; Pylkkänen, T.; Salvestrini, P.; Monaco, G.; Onida, G.; Reining, L. Dynamical response function in sodium and aluminum from time-dependent density-functional theory. *Phys. Rev. B: Condens. Matter Mater. Phys.* **2011**, *84*, 075109.
(28) Alkauskas, A.; Schneider, S. D.; Hébert, C.; Sagmeister, S.; Draxl, C. Dynamic structure factors of Cu, Ag, and Au: Comparative study from first principles. *Phys. Rev. B: Condens. Matter Mater. Phys.* **2013**, *88*, 195124.
(29) Campillo, I.; Rubio, A.; Pitarke, J. M. Ab initio calculations of the dynamical response of copper. *Phys. Rev. B: Condens. Matter Mater. Phys.* **1999**, *59*, 12188−12191.
(30) *Frontiers and Challenges in Warm Dense Matter*; Graziani, F., Desjarlais, M. P., Redmer, R., Trickey, S. B., Eds.; Springer International Publishing, 2014.
(31) Bonitz, M.; Dornheim, T.; Moldabekov, Z. A.; Zhang, S.; Hamann, P.; Kählert, H.; Filinov, A.; Ramakrishna, K.; Vorberger, J. Ab initio simulation of warm dense matter. *Phys. Plasmas* **2020**, *27*, 042710.
(32) Dornheim, T.; Moldabekov, Z. A.; Ramakrishna, K.; Tolias, P.; Baczewski, A. D.; Kraus, D.; Preston, T. R.; Chapman, D. A.; Böhme, M. P.; Döppner, T.; Graziani, F.; Bonitz, M.; Cangi, A.; Vorberger, J. Electronic density response of warm dense matter. *Phys. Plasmas* **2023**, *30*, 032705.
(33) Kritcher, A. L.; Swift, D. C.; Döppner, T.; Bachmann, B.; Benedict, L. X.; Collins, G. W.; DuBois, J. L.; Elsner, F.; Fontaine, G.; Gaffney, J. A.; Hamel, S.; Lazicki, A.; Johnson, W. R.; Kostinski, N.; Kraus, D.; MacDonald, M. J.; Maddox, B.; Martin, M. E.; Neumayer, P.; Nikroo, A.; Nilsen, J.; Remington, B. A.; Saumon, D.; Sterne, P. A.; Sweet, W.; Correa, A. A.; Whitley, H. D.; Falcone, R. W.; Glenzer, S. H. A measurement of the equation of state of carbon envelopes of white dwarfs. *Nature* **2020**, *584*, 51−54.
(34) Becker, A.; Lorenzen, W.; Fortney, J. J.; Nettelmann, N.; Schöttler, M.; Redmer, R. Ab initio equations of state for hydrogen (H-REOS.3) and helium (He-REOS.3) and their implications for the interior of brown dwarfs. *Astrophys. J., Suppl. Ser.* **2014**, *215*, 21.
(35) Fortov, V. E. Extreme states of matter on Earth and in space. *Phys.-Usp.* **2009**, *52*, 615−647.
(36) Betti, R.; Hurricane, O. A. Inertial-confinement fusion with lasers. *Nat. Phys.* **2016**, *12*, 435−448.
(37) MacDonald, M. J.; Saunders, A. M.; Bachmann, B.; Bethkenhagen, M.; Divol, L.; Doyle, M. D.; Fletcher, L. B.; Glenzer, S. H.; Kraus, D.; Landen, O. L.; LeFevre, H. J.; Klein, S. R.; Neumayer, P.; Redmer, R.; Schörner, M.; Whiting, N.; Falcone, R. W.; Döppner, T. Demonstration of a laser-driven, narrow spectral bandwidth x-ray source for collective x-ray scattering experiments. *Phys. Plasmas* **2021**, *28*, 032708.
(38) Ullrich, C. A. *Time-Dependent Density-Functional Theory: Concepts and Applications*; Oxford University Press, 2011.
(39) Kubo, R. The fluctuation-dissipation theorem. *Rep. Prog. Phys.* **1966**, *29*, 255−284.
(40) Giuliani, G.; Vignale, G. *Quantum Theory of the Electron Liquid*; Cambridge University Press: Cambridge, 2008.
(41) Gurtubay, I. G.; Pitarke, J. M.; Ku, W.; Eguiluz, A. G.; Larson, B. C.; Tischler, J.; Zschack, P.; Finkelstein, K. D. Electron-hole and plasmon excitations in 3*d* transition metals: Ab initio calculations and inelastic x-ray scattering measurements. *Phys. Rev. B: Condens. Matter Mater. Phys.* **2005**, *72*, 125117.
(42) Moldabekov, Z. A.; Pavanello, M.; Böhme, M. P.; Vorberger, J.; Dornheim, T. Linear-response time-dependent density functional theory approach to warm dense matter with adiabatic exchange-correlation kernels. *Phys. Rev. Res.* **2023**, *5*, 023089.
(43) Moldabekov, Z. A.; Vorberger, J.; Lokamani, M.; Dornheim, T. Averaging over atom snapshots in linear-response TDDFT of disordered systems: A case study of warm dense hydrogen. *J. Chem. Phys.* **2023**, *159*, 014107.
(44) Martin, R. M.; Reining, L.; Ceperley, D. M. *Interacting Electrons: Theory and Computational Approaches*; Cambridge University Press, 2016.
(45) Hybertsen, M. S.; Louie, S. G. Ab initio static dielectric matrices from the density-functional approach. I. Formulation and application to semiconductors and insulators. *Phys. Rev. B: Condens. Matter Mater. Phys.* **1987**, *35*, 5585−5601.
(46) Byun, Y.-M.; Sun, J.; Ullrich, C. A. Time-dependent density-functional theory for periodic solids: assessment of excitonic exchange−correlation kernels. *Electron. Struct.* **2020**, *2*, 023002.

https://doi.org/10.1021/acsomega.4c02920
ACS Omega 2024, 9, 25239−25250

(47) Gross, E. K. U.; Kohn, W. Local density-functional theory of frequency-dependent linear response. *Phys. Rev. Lett.* **1985**, *55*, 2850−2852.
(48) Silaeva, E. P.; Bevillon, E.; Stoian, R.; Colombier, J. P. Ultrafast electron dynamics and orbital-dependent thermalization in photo-excited metals. *Phys. Rev. B* **2018**, *98*, 094306.
(49) Baczewski, A. D.; Shulenburger, L.; Desjarlais, M. P.; Hansen, S. B.; Magyar, R. J. X-ray Thomson Scattering in Warm Dense Matter without the Chihara Decomposition. *Phys. Rev. Lett.* **2016**, *116*, 115004.
(50) Quong, A. A.; Eguiluz, A. G. First-principles evaluation of dynamical response and plasmon dispersion in metals. *Phys. Rev. Lett.* **1993**, *70*, 3955−3958.
(51) Weissker, H.-C.; Serrano, J.; Huotari, S.; Bruneval, F.; Sottile, F.; Monaco, G.; Krisch, M.; Olevano, V.; Reining, L. Signatures of Short-Range Many-Body Effects in the Dielectric Function of Silicon for Finite Momentum Transfer. *Phys. Rev. Lett.* **2006**, *97*, 237602.
(52) Weissker, H.-C.; Serrano, J.; Huotari, S.; Luppi, E.; Cazzaniga, M.; Bruneval, F.; Sottile, F.; Monaco, G.; Olevano, V.; Reining, L. Dynamic structure factor and dielectric function of silicon for finite momentum transfer: Inelastic x-ray scattering experiments and ab initio calculations. *Phys. Rev. B: Condens. Matter Mater. Phys.* **2010**, *81*, 085104.
(53) Moldabekov, Z. A.; Lokamani, M.; Vorberger, J.; Cangi, A.; Dornheim, T. Non-empirical Mixing Coefficient for Hybrid XC Functionals from Analysis of the XC Kernel. *J. Phys. Chem. Lett.* **2023**, *14*, 1326−1333.
(54) Moldabekov, Z.; Böhme, M.; Vorberger, J.; Blaschke, D.; Dornheim, T. Ab Initio Static Exchange−Correlation Kernel across Jacob's Ladder without Functional Derivatives. *J. Chem. Theory Comput.* **2023**, *19*, 1286−1299.
(55) Krane, K. Dispersion and damping of volume plasmons in polycrystalline aluminium and indium. *J. Phys. F: Met. Phys.* **1978**, *8*, 2133−2137.
(56) Sprösser-Prou, J.; Vom Felde, A.; Fink, J. Aluminum bulk-plasmon dispersion and its anisotropy. *Phys. Rev. B: Condens. Matter Mater. Phys.* **1989**, *40*, 5799−5801.
(57) Brydson, R. *Electron Energy Loss Spectroscopy*; CRC Press, 2020.
(58) Cho, B. I.; Ogitsu, T.; Engelhorn, K.; Correa, A. A.; Ping, Y.; Lee, J. W.; Bae, L. J.; Prendergast, D.; Falcone, R. W.; Heimann, P. A. Measurement of Electron-Ion Relaxation in Warm Dense Copper. *Sci. Rep.* **2016**, *6*, 18843.
(59) Cho, B. I.; Engelhorn, K.; Correa, A. A.; Ogitsu, T.; Weber, C. P.; Lee, H. J.; Feng, J.; Ni, P. A.; Ping, Y.; Nelson, A. J.; Prendergast, D.; Lee, R. W.; Falcone, R. W.; Heimann, P. A. Electronic Structure of Warm Dense Copper Studied by Ultrafast X-Ray Absorption Spectroscopy. *Phys. Rev. Lett.* **2011**, *106*, 167601.
(60) Jourdain, N.; Lecherbourg, L.; Recoules, V.; Renaudin, P.; Dorchies, F. Ultrafast Thermal Melting in Nonequilibrium Warm Dense Copper. *Phys. Rev. Lett.* **2021**, *126*, 065001.
(61) Smirnov, N. A. Copper, gold, and platinum under femtosecond irradiation: Results of first-principles calculations. *Phys. Rev. B* **2020**, *101*, 094103.
(62) Nicoul, M.; Shymanovich, U.; Tarasevitch, A.; von der Linde, D.; Sokolowski-Tinten, K. Picosecond acoustic response of a laser-heated gold-film studied with time-resolved x-ray diffraction. *Appl. Phys. Lett.* **2011**, *98*, 191902.
(63) White, T. G.; Mabey, P.; Gericke, D. O.; Hartley, N. J.; Doyle, H. W.; McGonegle, D.; Rackstraw, D. S.; Higginbotham, A.; Gregori, G. Electron-phonon equilibration in laser-heated gold films. *Phys. Rev. B: Condens. Matter Mater. Phys.* **2014**, *90*, 014305.
(64) Recoules, V.; Clérouin, J.; Zérah, G.; Anglade, P. M.; Mazevet, S. Effect of Intense Laser Irradiation on the Lattice Stability of Semiconductors and Metals. *Phys. Rev. Lett.* **2006**, *96*, 055503.
(65) Mortensen, J. J.; Hansen, L. B.; Jacobsen, K. W. Real-space grid implementation of the projector augmented wave method. *Phys. Rev. B: Condens. Matter Mater. Phys.* **2005**, *71*, 035109.
(66) Enkovaara, J.; Rostgaard, C.; Mortensen, J. J.; Chen, J.; Dułak, M.; Ferrighi, L.; Gavnholt, J.; Glinsvad, C.; Haikola, V.; Hansen, H. A.; Kristoffersen, H. H.; Kuisma, M.; Larsen, A. H.; Lehtovaara, L.; Ljungberg, M.; Lopez-Acevedo, O.; Moses, P. G.; Ojanen, J.; Olsen, T.; Petzold, V.; Romero, N. A.; Stausholm-Møller, J.; Strange, M.; Tritsaris, G. A.; Vanin, M.; Walter, M.; Hammer, B.; Häkkinen, H.; Madsen, G. K. H.; Nieminen, R. M.; Nørskov, J. K.; Puska, M.; Rantala, T. T.; Schiøtz, J.; Thygesen, K. S.; Jacobsen, K. W. Electronic structure calculations with GPAW: a real-space implementation of the projector augmented-wave method. *J. Phys.: Condens. Matter* **2010**, *22*, 253202.
(67) Walter, M.; Häkkinen, H.; Lehtovaara, L.; Puska, M.; Enkovaara, J.; Rostgaard, C.; Mortensen, J. J. Time-dependent density-functional theory in the projector augmented-wave method. *J. Chem. Phys.* **2008**, *128*, 244101.
(68) Yan, J.; Mortensen, J. J.; Jacobsen, K. W.; Thygesen, K. S. Linear density response function in the projector augmented wave method: Applications to solids, surfaces, and interfaces. *Phys. Rev. B: Condens. Matter Mater. Phys.* **2011**, *83*, 245122.
(69) Hjorth Larsen, A.; Jørgen Mortensen, J.; Blomqvist, J.; Castelli, I. E.; Christensen, R.; Dułak, M.; Friis, J.; Groves, M. N.; Hammer, B.; Hargus, C.; Hermes, E. D.; Jennings, P. C.; Bjerre Jensen, P.; Kermode, J.; Kitchin, J. R.; Leonhard Kolsbjerg, E.; Kubal, J.; Kaasbjerg, K.; Lysgaard, S.; Bergmann Maronsson, J.; Maxson, T.; Olsen, T.; Pastewka, L.; Peterson, A.; Rostgaard, C.; Schiøtz, J.; Schütt, O.; Strange, M.; Thygesen, K. S.; Vegge, T.; Vilhelmsen, L.; Walter, M.; Zeng, Z.; Jacobsen, K. W. The atomic simulation environment—a Python library for working with atoms. *J. Phys.: Condens. Matter* **2017**, *29*, 273002.
(70) Bahn, S. R.; Jacobsen, K. W. An object-oriented scripting interface to a legacy electronic structure code. *Comput. Sci. Eng.* **2002**, *4*, 56−66.
(71) Blöchl, P. E. Projector augmented-wave method. *Phys. Rev. B: Condens. Matter Mater. Phys.* **1994**, *50*, 17953−17979.
(72) Perdew, J. P.; Wang, Y. Accurate and simple analytic representation of the electron-gas correlation energy. *Phys. Rev. B: Condens. Matter Mater. Phys.* **1992**, *45*, 13244−13249.
(73) Wyckoff, R. W. G. *Crystal Structures*; Interscience Publishers: New York, 1963.
(74) Mahan, G. *Many-Particle Physics*; *Physics of Solids and Liquids*; Springer US, 1990.
(75) Bohm, D.; Gross, E. P. Theory of Plasma Oscillations. A. Origin of Medium-Like Behavior. *Phys. Rev.* **1949**, *75*, 1851−1864.
(76) Hamann, P.; Vorberger, J.; Dornheim, T.; Moldabekov, Z. A.; Bonitz, M. Ab initio results for the plasmon dispersion and damping of the warm dense electron gas. *Contrib. Plasma Phys.* **2020**, *60*, No. e202000147.
(77) Ott, T.; Thomsen, H.; Abraham, J. W.; Dornheim, T.; Bonitz, M. Recent progress in the theory and simulation of strongly correlated plasmas: phase transitions, transport, quantum, and magnetic field effects. *Eur. Phys. J. D* **2018**, *72*, 84.
(78) Kraus, D.; Ravasio, A.; Gauthier, M.; Gericke, D. O.; Vorberger, J.; Frydrych, S.; Helfrich, J.; Fletcher, L. B.; Schaumann, G.; Nagler, B.; Barbrel, B.; Bachmann, B.; Gamboa, E. J.; Göde, S.; Granados, E.; Gregori, G.; Lee, H. J.; Neumayer, P.; Schumaker, W.; Döppner, T.; Falcone, R. W.; Glenzer, S. H.; Roth, M. Nanosecond formation of diamond and lonsdaleite by shock compression of graphite. *Nat. Commun.* **2016**, *7*, 10970.
(79) Lazicki, A.; McGonegle, D.; Rygg, J. R.; Braun, D. G.; Swift, D. C.; Gorman, M. G.; Smith, R. F.; Heighway, P. G.; Higginbotham, A.; Suggit, M. J.; Fratanduono, D. E.; Coppari, F.; Wehrenberg, C. E.; Kraus, R. G.; Erskine, D.; Bernier, J. V.; McNaney, J. M.; Rudd, R. E.; Collins, G. W.; Eggert, J. H.; Wark, J. S. Metastability of diamond ramp-compressed to 2 terapascals. *Nature* **2021**, *589*, 532−535.
(80) Mo, M. Z.; Chen, Z.; Li, R. K.; Dunning, M.; Witte, B. B. L.; Baldwin, J. K.; Fletcher, L. B.; Kim, J. B.; Ng, A.; Redmer, R.; Reid, A. H.; Shekhar, P.; Shen, X. Z.; Shen, M.; Sokolowski-Tinten, K.; Tsui, Y. Y.; Wang, Y. Q.; Zheng, Q.; Wang, X. J.; Glenzer, S. H. Heterogeneous to homogeneous melting transition visualized with ultrafast electron diffraction. *Science* **2018**, *360*, 1451−1455.

https://doi.org/10.1021/acsomega.4c02920
ACS Omega 2024, 9, 25239−25250

(81) Chen, Z.; Holst, B.; Kirkwood, S. E.; Sametoglu, V.; Reid, M.; Tsui, Y. Y.; Recoules, V.; Ng, A. Evolution of ac Conductivity in Nonequilibrium Warm Dense Gold. *Phys. Rev. Lett.* **2013**, *110*, 135001.
(82) Liu, S.; Grech, C.; Guetg, M.; Karabekyan, S.; Kocharyan, V.; Kujala, N.; Lechner, C.; Long, T.; Mirian, N.; Qin, W.; Serkez, S.; Tomin, S.; Yan, J.; Abeghyan, S.; Anton, J.; Blank, V.; Boesenberg, U.; Brinker, F.; Chen, Y.; Decking, W.; Dong, X.; Kearney, S.; La Civita, D.; Madsen, A.; Maltezopoulos, T.; Rodriguez-Fernandez, A.; Saldin, E.; Samoylova, L.; Scholz, M.; Sinn, H.; Sleziona, V.; Shu, D.; Tanikawa, T.; Terentiev, S.; Trebushinin, A.; Tschentscher, T.; Vannoni, M.; Wohlenberg, T.; Yakopov, M.; Geloni, G. Cascaded hard X-ray self-seeded free-electron laser at megahertz repetition rate. *Nat. Photonics* **2023**, *17*, 984−991.
(83) Hara, T.; Inubushi, Y.; Katayama, T.; Sato, T.; Tanaka, H.; Tanaka, T.; Togashi, T.; Togawa, K.; Tono, K.; Yabashi, M.; et al. Two-colour hard X-ray free-electron laser with wide tunability. *Nat. Commun.* **2013**, *4*, 2919.
(84) Inoue, I.; Osaka, T.; Hara, T.; Yabashi, M. Two-color X-ray free-electron laser consisting of broadband and narrowband beams. *J. Synchrotron Radiat.* **2020**, *27*, 1720−1724.
(85) Kraus, D.; Bachmann, B.; Barbrel, B.; Falcone, R. W.; Fletcher, L. B.; Frydrych, S.; Gamboa, E. J.; Gauthier, M.; Gericke, D. O.; Glenzer, S. H.; Göde, S.; Granados, E.; Hartley, N. J.; Helfrich, J.; Lee, H. J.; Nagler, B.; Ravasio, A.; Schumaker, W.; Vorberger, J.; Döppner, T. Characterizing the ionization potential depression in dense carbon plasmas with high-precision spectrally resolved x-ray scattering. *Plasma Phys. Controlled Fusion* **2019**, *61*, 014015.
(86) Böhme, M. P.; Fletcher, L. B.; Döppner, T.; Kraus, D.; Baczewski, A. D.; Preston, T. R.; MacDonald, M. J.; Graziani, F. R.; Moldabekov, Z. A.; Vorberger, J.; Dornheim, T. Evidence of free-bound transitions in warm dense matter and their impact on equation-of-state measurements. *arXiv* **2023**, arXiv:2306.17653.
(87) Kozlowski, J.; Perchak, D.; Burke, K. Generalized Gradient Approximation Made Thermal. *arXiv* **2023**, arXiv:2308.03319.
(88) Karasiev, V. V.; Dufty, J. W.; Trickey, S. B. Nonempirical Semilocal Free-Energy Density Functional for Matter under Extreme Conditions. *Phys. Rev. Lett.* **2018**, *120*, 076401.
(89) Karasiev, V. V.; Sjostrom, T.; Dufty, J.; Trickey, S. B. Accurate Homogeneous Electron Gas Exchange-Correlation Free Energy for Local Spin-Density Calculations. *Phys. Rev. Lett.* **2014**, *112*, 076403.
(90) Groth, S.; Dornheim, T.; Sjostrom, T.; Malone, F. D.; Foulkes, W. M. C.; Bonitz, M. Ab initio Exchange−Correlation Free Energy of the Uniform Electron Gas at Warm Dense Matter Conditions. *Phys. Rev. Lett.* **2017**, *119*, 135001.
(91) Dornheim, T.; Groth, S.; Bonitz, M. The uniform electron gas at warm dense matter conditions. *Phys. Rep.* **2018**, *744*, 1−86.
(92) Karasiev, V. V.; Calderin, L.; Trickey, S. B. Importance of finite-temperature exchange correlation for warm dense matter calculations. *Phys. Rev. E* **2016**, *93*, 063207.
(93) Dornheim, T.; Groth, S.; Vorberger, J.; Bonitz, M. Ab initio Path Integral Monte Carlo Results for the Dynamic Structure Factor of Correlated Electrons: From the Electron Liquid to Warm Dense Matter. *Phys. Rev. Lett.* **2018**, *121*, 255001.

https://doi.org/10.1021/acsomega.4c02920
ACS Omega 2024, 9, 25239−25250